

# Correlated optical and electron microscopy reveal the role of multiple defect species and local strain on quantum emission

Fariah Hayee<sup>1\*</sup>, Leo Yu<sup>2</sup>, Jingyuan Linda Zhang<sup>3</sup>, Christopher J. Ciccarino<sup>4</sup>, Minh Nguyen<sup>5</sup>, Ann F Marshall<sup>6</sup>, Igor Aharonovich<sup>5</sup>, Jelena Vučković<sup>3</sup>, Prineha Narang<sup>4</sup>, Tony F. Heinz<sup>2</sup>, Jennifer A Dionne<sup>7\*</sup>

<sup>1</sup>*Department of Electrical Engineering, Stanford University, 450 Serra Mall, Stanford, CA 94305, USA*

<sup>2</sup>*Department of Applied Physics, Stanford University, Stanford, CA 94305, USA*

<sup>3</sup>*E. L. Ginzton Laboratory, Stanford University, Stanford, CA 94305, USA*

<sup>4</sup>*John A. Paulson School of Engineering and Applied Sciences, Harvard University, Cambridge, MA 02138, USA*

<sup>5</sup>*Biomedical Materials and Devices, University of Technology Sydney, Ultimo, NSW, 2007, Australia*

<sup>6</sup>*Stanford Nano Shared Facilities, Stanford University, Stanford, CA 94305, USA*

<sup>7</sup>*Department of Materials Science and Engineering, Stanford University, Stanford, CA 94305, USA*

*e-mail: fariah@stanford.edu; jdionne@stanford.edu*

**Color-centers in solids have emerged as promising candidates for quantum photonic computing,<sup>1,2</sup> communications,<sup>3,4</sup> and sensing<sup>5-7</sup> applications. Defects in hexagonal boron nitride (hBN) possess high-brightness, room-temperature quantum emission,<sup>8-10</sup> but their large spectral variability and unknown local structure significantly challenge their technological utility. Here, we directly correlate hBN quantum emission with its local, atomic-scale crystalline structure using correlated photoluminescence (PL) and cathodoluminescence (CL) spectroscopy. Across 20 emitters, we observe zero phonon lines (ZPLs) in PL and CL ranging from 540-720 nm. CL mapping reveals that multiple defects and distinct defect species located within an optically-diffraction-limited region can each contribute to the observed PL spectra. Through high resolution transmission electron imaging, we find that emitters are located in regions with multiple fork-like dislocations. Additionally, local strain maps indicate that strain is not responsible for observed ZPL spectral range, though it can enable spectral tuning of particular emitters. While many emitters have identical ZPLs in CL and PL, others exhibit reversible but distinct CL and PL peaks; density functional calculations indicate that defect complexes and charge-state transitions influence such emission spectra. Our results highlight the sensitivity of defect-driven quantum emission to the surrounding crystallography, providing a foundation for atomic-scale optical characterization.**

Defects in hexagonal boron nitride (hBN) exhibit promising quantum-optical properties including high photostability,<sup>11,12</sup> narrow linewidth,<sup>9</sup> high brightness,<sup>8</sup> and high emission into the zero phonon line (ZPL).<sup>13</sup> However, both intrinsic and engineered defects in mono- and multi-layer

films exhibit large spectral variability.<sup>14–16</sup> Additionally, some emitters exhibit distinct polarization profiles for absorption and emission<sup>17</sup> as well as different quantum efficiencies for different excitation wavelengths, suggesting a complicated electronic structure.<sup>11,12,18</sup> Establishing correlation between the emission of the defect and its local crystallographic structure can address outstanding fundamental questions about hBN color centers and accelerate their technological development.

Recent progress in super-resolution optical microscopy and cathodoluminescence (CL) spectroscopy has enabled localization of radiative emission beyond the diffraction limit. For example, quantum emission from hBN has been visualized with 10 nm and 80 nm spatial resolution using super-resolution techniques<sup>19</sup> and CL spectroscopy<sup>20</sup>, respectively. However, to date, these techniques have not provided the requisite resolution to correlate quantum emission with local crystallographic structure, including strain and defects. Aberration-corrected electron microscopy<sup>21,22</sup> and scanning tunneling microscopy<sup>23–25</sup> have revealed individual defect structures in mono- and multi-layer samples, but without correlation to the defects optical signatures. Notably, locating color centers within an electron microscope can be extremely challenging, requiring correlated optical and structural maps that span nearly four orders of magnitude.

Here, we correlate confocal PL and CL spectroscopy of hBN quantum emitters with their nano-to-atomic-scale structure using scanning transmission electron microscopy (STEM). First, we establish a direct correlation between a defect’s PL and CL emission, showing two classes of stable emitters: those for which both electron-beam excitation and 532-nm laser excitation generate similar optical spectra, and those for which distinct but reversible CL and PL peaks emerge. Focusing on emitters with identical PL and CL, we use hyperspectral STEM-CL mapping and find that multiple radiative defects are localized within a  $\sim 50$  nm region. Accordingly, defect-defect interactions and/or multiple radiative transitions within the joint density of electronic states can influence the far-field PL spectra. Through high-resolution electron imaging, we find that the optically brightest regions have a high density of defects and dislocations. Diffraction also reveals that strain is not responsible for the large spectral variability of observed ZPLs, though it can enable tunability of some emitters.

Our experimental STEM-CL setup is depicted in Fig. 1(a). A hBN multi-layer (1-5 layers) nanoflake solution in ethanol and water is drop-cast on a holey carbon TEM substrate for PL, CL and TEM imaging. First, we identify emission centers in multilayer hBN flakes using confocal PL mapping with a 532 nm excitation laser. With sub-bandgap excitation<sup>26</sup>, we excite deep-band defects. We find bright emission ranging between 540-720 nm, with spectral full-widths at half-max (FWHM) ranging from 4 to 12 nm at room temperature. Figure 1(b) and (c) include an optical micrograph, PL map and PL spectrum of one such representative emitter with a ZPL of 582 nm and two phonon replicas at 622.5 and 680.7 nm (separated by 139 meV and 161 meV from the ZPL). We verify that the emission lines are indeed of single-photon nature by characterizing the second-order autocorrelation function  $g^{(2)}(\tau)$  using a Hanbury Brown and Twiss (HBT) setup. Without background correction, the  $g^{(2)}(\tau)$  dip at zero delay time  $\tau=0$  is below 0.5 (Fig. 1c inset), confirming the non-classical nature of the emission. The PL emission spectra and  $g^{(2)}$  of 4 additional

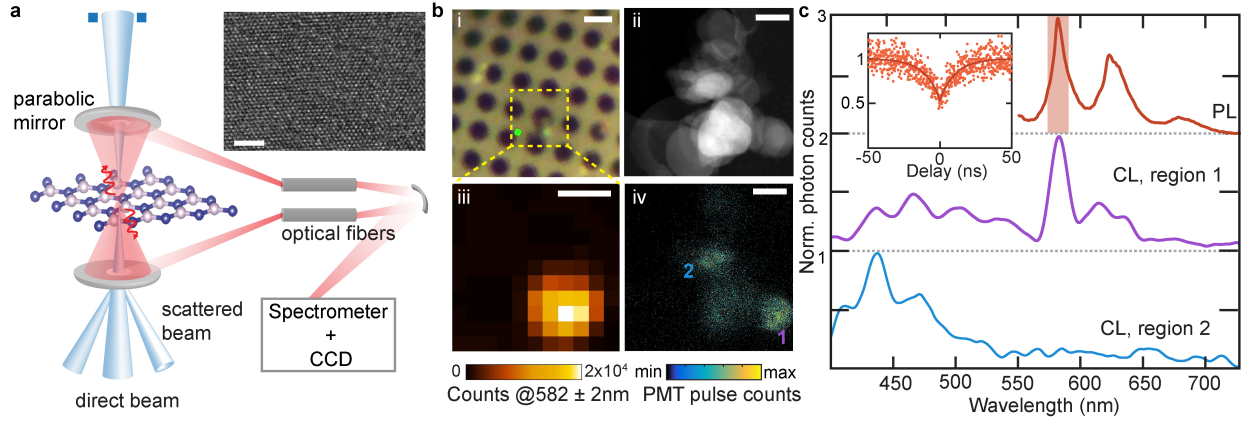


**Figure 1: Correlated optical and electron characterization of quantum emitters in hBN.** (a) Schematic illustration of the cathodoluminescence setup in a TEM. Two parabolic mirrors surround the sample, and the resulting signal is collected via optical fibers and directed to a spectrometer. An alternate light path to a PMT (not shown) can be selected by changing the mirror position. The inset shows a high-resolution TEM image of the sample. Scale bar is 2 nm. (b) Optical image (i) and photoluminescence map (iii) at 582 nm; STEM-HAADF image (ii) and panchromatic CL map (iv) of the **same** hBN flake on a holey-carbon TEM grid. Scale bars are 1 μm for the optical images and 200 nm for the STEM images. (c) PL spectrum at the optical hotspot and CL spectra at the regions marked in (b). The corresponding  $g^{(2)}$  curve is plotted in the inset. The vertical shaded area in the PL spectrum corresponds to the studied ZPL. The  $g^{(2)}$  measurement is not background corrected.

emitters can be found in the supporting information.

We next identify the same emitters in the TEM (see methods). As seen in Fig. 1(a), we use a focused electron probe (typical diameter of 1.5 nm) and collect the emitted light using two parabolic mirrors positioned above and below the sample. A spectrometer and CCD enable spectroscopic mapping of defects correlated with high-resolution transmission electron microscopy. An alternate light path with a photomultiplier tube (PMT) is used to rapidly map panchromatic emission. A high-angle annular dark field (HAADF) image and corresponding panchromatic-CL (pan-CL) image is shown in Fig. 1(b). The HAADF image shows multiple overlapping nanoflakes, where the thickest nanoflake-stack appears the brightest. As seen from Fig. 1b panels (iii) and (iv), within the region of brightest PL, the pan-CL image has two main emission ‘hotspots’. We collect spectral signatures from each region, with representative point-spectra shown in Fig. 1(c). We find that for this particular nanoflake, the CL spectra of region 1 matches well with the PL spectra whereas region 2 has a broad spectral peak at 420 nm that is prevalent throughout this flake as well as in many additional flakes. The ZPL in region 1 has a broader FWHM in the CL spectrum (10 nm) than the PL spectrum (6 nm), a consequence of the CL spectrometer resolution ( $\sim 10$  nm). In addition to the ZPL, two other CL peaks are seen at 614 nm and 633 nm; as will be shown later, the first is from another nearby defect while the second is a phonon sideband.

We zoom into region 1 of Figure 1b(iv) and use hyperspectral CL imaging to map local emission with  $\sim 30$  nm spatial resolution. Figure 2a shows a HAADF image of region 1, where the intensity corresponds to the number of flakes (i.e., different sample thicknesses). CL spectra are collected in 5 nm spatial increments throughout the region denoted by the white dotted box (see methods for details). The three principal CL spectra and their corresponding spatial maps are included in Fig. 2a. As seen, one constituent spectrum exhibits a 582 nm ZPL, shown by the red spectrum and the red-colored spectral weight map (labelled  $c_1$ ). This emitter is a single-photon emitter, with PL and CL that closely match. Two additional emitters are located within 30 and 80 nm of this central emitter, respectively: one emitter is near the top of the mapped region, with a peak emission at 614 nm (purple map,  $c_2$ ), while the other is near the bottom right with a peak emission at 600 nm (blue map,  $c_3$ ). The centroid of each emitter is boxed on the HAADF image. Interestingly, the 600 nm emitter (blue rectangle) is situated in a region where thickness of the stack changes, indicating a nanoflake edge.

The spectrum of Fig. 2a/ $c_1$  also illustrates a recurring emission profile with four higher energy peaks at 433, 461, 490 and 532 nm. We have related these blue higher energy peaks in 3 spatially-distinct but spectrally-similar signatures single-photon emitter CL spectra (see SI), all with ZPL peaks at 578-590 nm, with two possible phonon replicas in PL. In all three cases, the highest two energy peaks (433 and 461 nm) are separated by nearly the hBN phonon energy  $\sim 180$  meV). Such CL spectra could emerge from closely spaced (sub-20 nm) emitters and their phonon sidebands. The recurrent nature of the higher energy peaks suggests that such emitter(s) commonly accompany the 580 nm emitter.

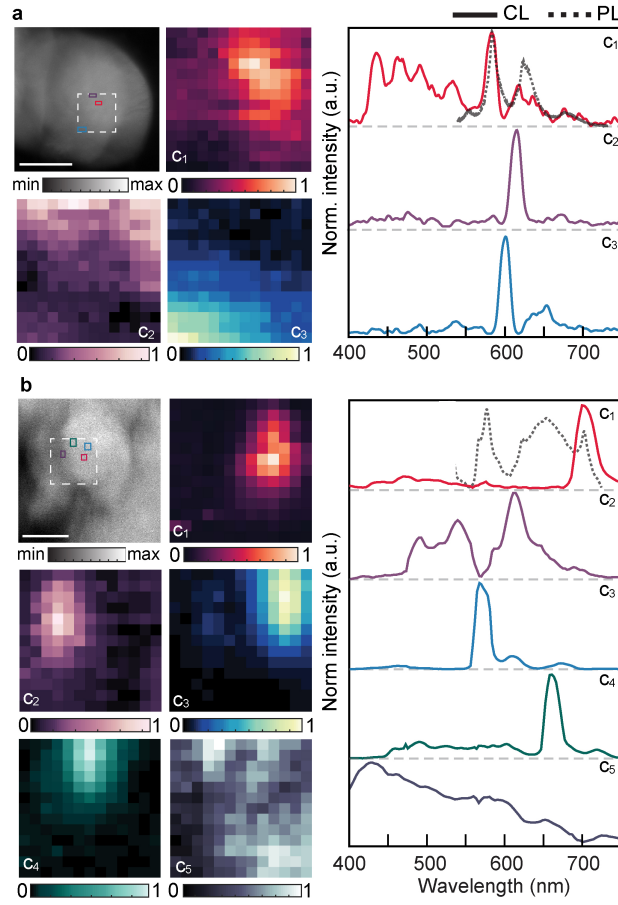


Figure 2: **Cathodoluminescence mapping reveals multiple and distinct quantum emitter species within a diffraction-limited optical spot** (a) STEM-HAADF image of region 1 in Fig. 1(b) and cathodoluminescence spectral weights (normalized to each component) of the white marked region. The red, purple, and teal colored boxes in the HAADF image are positions of the brightest pixels of the  $c_1$ ,  $c_2$  and  $c_3$  spectral components. The decomposed spectra are plotted next to the spectral weights. The PL spectrum of the corresponding hotspot is also plotted in black dotted line. Scale bar in the HAADF image is 100 nm and each pixel in the CL spectral map is 5 nm. (b) CL spectral maps of another region hosting two different quantum emitters at 571 nm and 704 nm. The PL spectrum is a result of multiple defects as seen through CL spectral weight mapping. Pixel size in the CL map is 14.8 nm and the scale bar in the HAADF image is 200 nm.

PL spectra can also, in some cases, result from multiple single-photon emitters within one diffraction-limited spot. Figure 2b illustrates one such case. As seen, the PL spectrum (black dotted line) exhibits two distinctive, sharp peaks at 571 nm and 704 nm. Through hyperspectral CL mapping, we see that the two emission lines are actually from two different emitters which are separated by 50 nm, shown in the blue and red CL maps respectively. The smaller PL peak at 625 nm is likely a combination of the 570 nm emitter phonon sideband (blue solid spectrum with a small peak at 620 nm) and an additional radiative defect active only in CL emitting at 625 nm (purple map). A fourth point defect at 682 nm is also evident upon electron beam excitation, shown in the green map. Finally, we observe broad emission peaking at 425-430 nm, a signal prevalent throughout most flakes and generally very delocalized. This broad ultraviolet emission can be associated with prevalent impurity atoms.

The spectral maps of Fig. 2 also provide an estimate of the carrier diffusion lengths. Linescans of intensity across particular defect centers are plotted in SI Fig. 8. We find that the emission intensity decreases to  $1/e$  of its maximum value at 30-120 nm for various emitters, which enables us to distinguish emitters with similar resolution. As will be shown below, the high density of structural defects and dislocations near emitters may account for such short diffusion lengths.

We leverage imaging and diffraction to reveal the nanoscale structure of the emitting regions, yielding important insights about the emitters' structure and local environment. Fig. 3(a) presents the HAADF image and CL spectral map for an emitter exhibiting a ZPL of 578 nm; Fig. 3(b) shows the corresponding CL and PL spectra. High-resolution TEM enables imaging of the emitting region and its immediate surroundings, shown in Fig. 3(c). Note that the brightest emitting region is marked with a black dotted line in both the CL map and the TEM image. As seen in the inset, the selected area electron diffraction of the region has one set of diffraction peaks; all flakes are oriented in the  $\langle 100 \rangle$ -direction without any noticeable lateral rotation. Thus, the lines at the top right corner of the emitting region TEM image (Fig. 3(c), near black dotted outline) are not grain boundaries, but rather flake edges. We then compare Fast Fourier Transform (FFT) maps of the emitting regions with those of the optically inactive regions. Intriguingly, the emission region has visible 'streaking', due to high dislocation densities (teal square region, Fig. 3d). The inverse FFT (IFFT) images, constructed by capturing a pair of FFT points (marked with white circle in the FFT images), show many stacking fault and fork-like dislocations in this region. This result is in contrast to other, non-emitting regions, which show no noticeable FFT streaking. Additional optically active regions are presented in the SI, where we observe both the presence of 'missing atom' type defects as well as nearby small lattice rotations (supported by a grain boundary or array of dislocations).

Our technique also allows correlation of optical emission with the region's local strain. We reconstruct strain maps of the emitting regions using nano-beam electron diffraction (NBED), collecting diffraction images every 2 nm (see SI for details). To estimate the local strain variation in multilayer hBN, we focus on regions without noticeable lateral rotation (that is, showing only one set of diffraction disks). The strain component maps of the region marked in Fig. 3(a) are presented

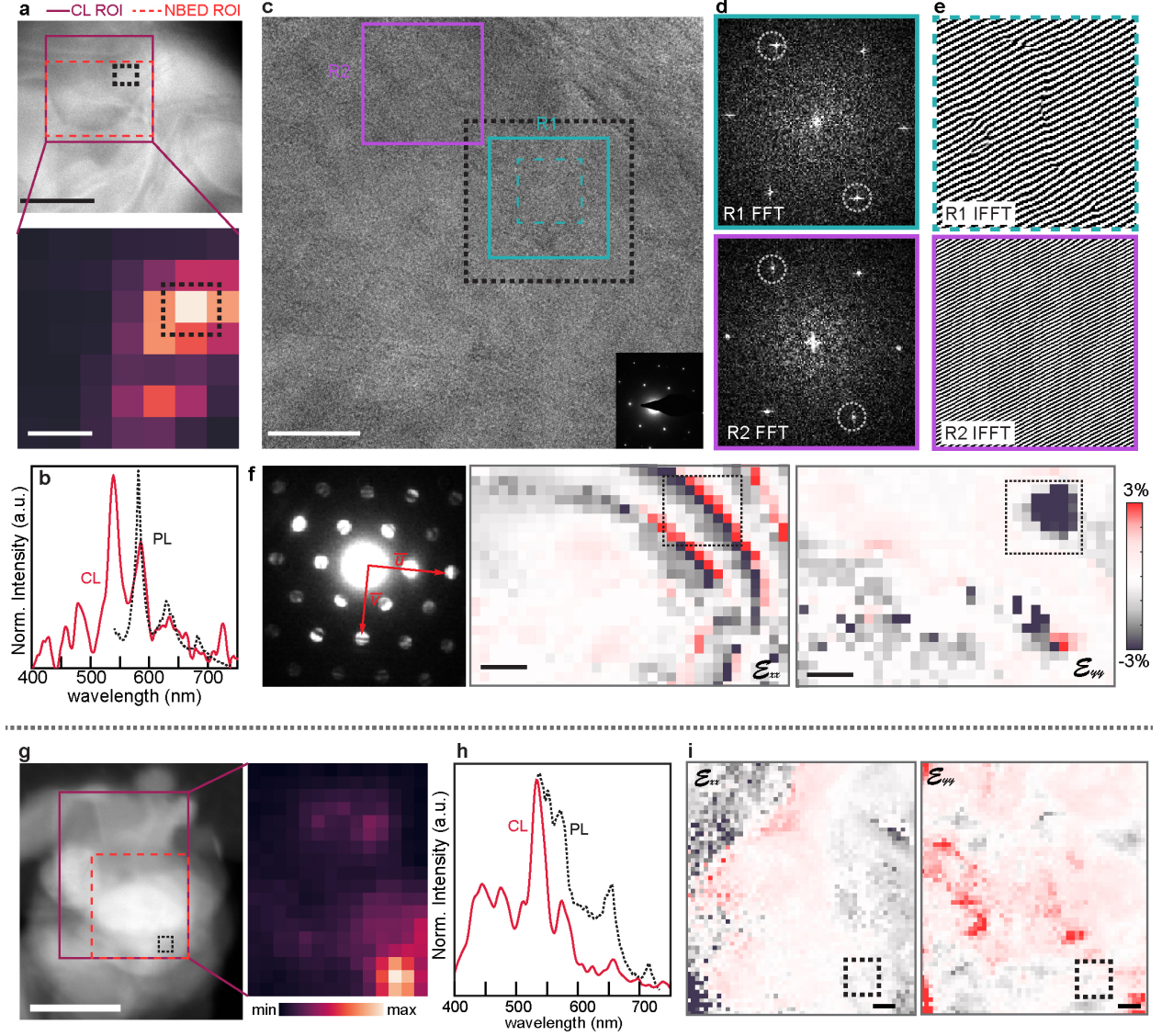


Figure 3: **Correlating quantum emission with local crystallographic structure and strain** (a-b) HAADF, CL spectral map, and corresponding PL and CL spectra of one emitter with a ZPL at 578 nm. The scale bar is 50 nm for the HAADF image and 20 nm for the CL spectral map. (c) TEM image where the optically-brightest pixel is marked by the black dotted line. The scale bar is 10 nm. (Inset) Selected area electron diffraction pattern of the entire region. (d) FFT patterns of the two marked regions in (c). (e) IFFT images of the two regions in (c), constructed by taking an image mask around the marked (100) pair of points in (d). Multiple fork dislocations are observed in the bright region. (f) The nano-beam electron diffraction pattern collected by averaging over a 35x35 pixel region and reconstructed strain maps for the region marked with the orange dotted rectangle in (a). The orthogonal vectors  $\vec{u}$  and  $\vec{v}$  are marked. The scale bar is 10 nm. (g-h) HAADF, CL map and corresponding PL and CL spectra of another emitter. The scale bar is 200 nm. (i) Strain maps along  $x$ - and  $y$ -directions show negligible strain in the optically bright pixels. Scale bar is 20 nm. The color bar is same as (f). The localization of the CL bright spot to the strain map (the dotted black box) has at most a 6 nm drift error in both the  $x$ - and  $y$ -directions (see SI).



in Fig. 3(f), where the position of the brightest pixel of the CL map is marked with the black dotted rectangle. As seen, a large strain variation in the hotspot is observed compared to the surrounding: the mean compressive strain is 1% with a standard deviation of 1.5% along the  $y$  direction and  $0.36\% \pm 0.6\%$  along the  $x$  direction. On the other hand, the emitter of Fig. 2(a) with a ZPL at 582 nm is localized in a relatively unstrained region with a mean strain variation of  $-0.2\%$  (SD = 0.18%) and  $-0.5\%$  (SD = 0.5%) along  $x$  and  $y$  directions, respectively (see SI Fig. 4(a)). While the error in strain mapping is relatively large (rms error 0.23% for  $\mathcal{E}_{xx}$  and  $\sim 0.54\%$  for  $\mathcal{E}_{yy}$  due to flake tilt in random directions), the observed variation (4 nm = 15 meV) between the ZPLs of these two emitters with similar spectral signatures can be due to this local strain variation. Such spectral variation upon externally-applied strain is consistent with previous reports.<sup>10,27</sup> Interestingly, theoretically predicted tunability (meV/% strain) is on the order of 50-100 meV/%, much larger than what we observe (see SI Fig. 1 and Ref. 10). Our theoretical calculations suggest that out-of-plane distortions could also impact emission, as they are known to compete with atomically flat configurations.<sup>28,29</sup> While large hBN sheets are expected to force defects to the in-plane configuration, the observed proximity to dislocations suggests that our nanoflakes could be sufficiently weakened to allow out-of-plane distortions.

As shown in Fig. 3(b), we also observe three peaks at 532 nm, 582 nm and 650 nm in a relatively unstrained region. Another emitter at 712 nm is also observed in a region where the mean absolute strain is  $\leq 0.2\%$  with SD  $\leq 0.6\%$  (SI Fig. 4(b)), indicating that strain is not a requisite condition for spectrally-variable emission. Indeed, the spectral separation between the 530 nm and 712 nm emission peaks is larger (0.5 eV) than the calculated tunability of emission by strain for known defects and defect complexes (see SI Fig. 1 and Ref. 10, 27), indicating several distinct defect species must be responsible for the observed emission range.

Finally, Fig. 4 presents a library of defects excited by both laser and electron-beam irradiation, all of which are repeatable and stable upon electron beam and laser irradiation. Across 20 measured color centers, we observe two distinct emitter classes, examples of which are plotted in the left and right columns of Fig. 4. The first class of emitters (left column) exhibits PL emission lines that are well-matched to CL emission lines ( $E_1$ - $E_6$  and  $E_9$ ). These PL spectra are readily reproduced after electron beam exposure. We note that there are certain peaks that do not appear in CL. For example, for  $E_1$ , the broader emission at 575 nm is red shifted in CL.

The second class of emitters has a very different CL signature from their PL. For these emitters, we collect CL signatures of all bright regions separately, as described for Fig. 1; however, none match the ZPL observed in PL. The second column of Fig. 4 plots the brightest CL signatures for these emitters. Most of these defects are not destroyed under the electron beam as we can reproduce them in PL after electron beam imaging, indicating that any electron-induced change in the environment is reversible. For example, the CL of  $E_6'$ ,  $E_7$  and  $E_8$  is red-shifted by 10 nm, but the original ZPL can be reproduced in PL after e-beam exposure. Possibly, the orbital wavefunction of such emitter energy level is more sensitive to external stimuli, including electron beam induced carrier screening or the local temperature. The 575 nm emitter ( $E_9$ ) is permanently altered



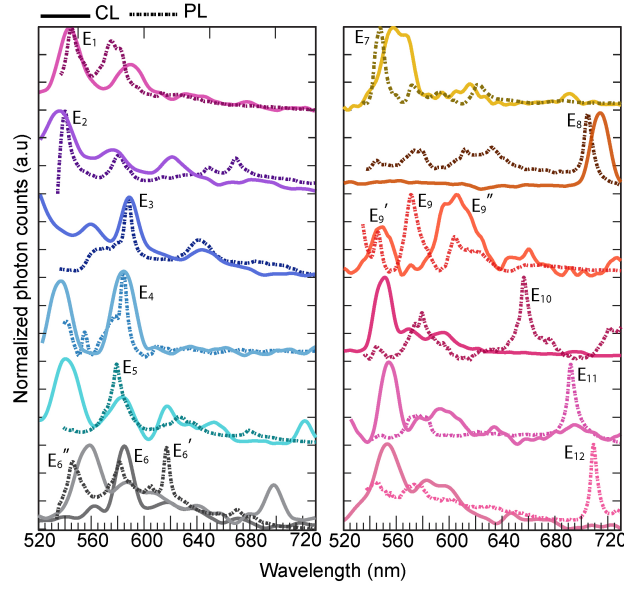


Figure 4: **Classifying two families of stable emitters with correlated photoluminescence and cathodoluminescence.** The first family of emitters, shown in the left column ( $E_1$ -  $E_6$ ) has closely-matched spectra upon optical and electron beam excitation. For  $E_6$  and  $E_6''$ , we plot two CL spectra given the broadly-separated PL peaks at 580nm and 530nm (see SI for details). The second family of emitters, shown in the right column, has distinct PL and CL, though the PL is reproducible after electron beam irradiation.  $E_7$ ,  $E_8$  and  $E_6''$  show slight spectral shifts in CL.  $E_9$  is altered permanently during electron beam exposure.

after electron-beam imaging, which can be due to the lower formation energy of the defect involved. ZPLs in the wavelength range 640-720 nm ( $E_{10}$ - $E_{12}$ ) are dim or not present under electron beam excitation, and their corresponding CL spectra show prominent peaks in the 540-550 nm range. This discrepancy between the PL and CL spectra could be due to a change in the emitter charge state<sup>11</sup>, or due to a nearby emitter that is not excited by 532-nm light but captures carriers competitively in the CL process.

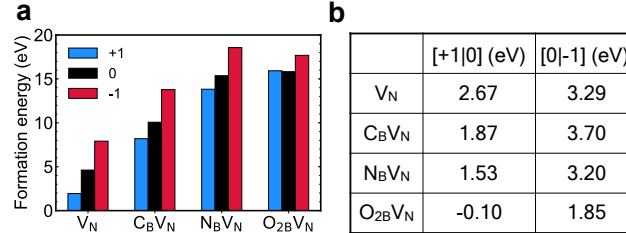


Figure 5: **First principles thermodynamic quantities for multilayer hBN.** (a) Fermi level formation energies calculated using the appropriate charge correction for four representative defects ( $V_N$ ,  $C_B V_N$ ,  $N_B V_N$  and  $O_{2B} V_N$ ) in various charge states, with corresponding charge transition levels shown in (b). Multi-component defects are found to have higher formation energies.

Together, our observations indicate that the quantum emitters are likely defect complexes and that the surrounding nanoscale structure must be taken into account to understand their electronic level structure. First, we note that the stability of defects under electron irradiation points toward higher-energy complexes. Using first-principles calculations based on density functional theory (DFT), we predict the formation energies for four defects ( $V_N$ ,  $C_B V_N$ ,  $N_B V_N$  and  $O_{2B} V_N$ ). As seen in Fig. 5a, multi-component defect complexes like  $N_B V_N$  and  $O_{2B} V_N$  are harder to form and therefore more resilient to electron beam exposure. Our results are consistent with recent theoretical work showing that simple impurities are highly mobile.<sup>30</sup> We hypothesize that electron-beam-stable defect complexes could form from merging of these mobile impurities; we also note that the 580 nm ZPL ( $E_3$ - $E_5$  in Fig. 4) has been associated with the neutral  $N_B V_N$  emitter in group-theory-based modeling<sup>31</sup> and previous DFT studies.<sup>8,10,32</sup> Our calculations also reveal multiple charge-state transition levels within the bandgap and at ultraviolet frequencies, shown in Fig. 5b. Such charge-state transitions are likely accessed more easily by electron excitation, for example through electron-beam charging of hBN and subsequent shifting of the local Fermi level. Interestingly, these charge-state transitions have significant impact on the defect orbital structure, as seen in SI Fig. 1. These charged-states possess a variety of possible excited state configurations, enabling many emission pathways and, accordingly, a multitude of spectral lines.

In conclusion, we have established a direct correlation between PL, CL, and local crystallographic structure of quantum emitters in hBN. CL hyperspectral mapping reveals multiple emitters within a diffraction-limited optical spot, each contributing to the PL spectra. High resolution electron imaging and diffraction indicate the presence of multiple stacking-fault and fork dislocations in the optical hotspot. Further, the large spectral variability of the ZPLs is not due to strain, but rather more likely the multiple defect species and complexes. Importantly, most of the emitters

are stable upon electron and optical irradiation. Beyond structure-function correlations, our results point to the intriguing possibility of electrically exciting quantum emitters. Looking forward, we envision Angstrom-scale imaging of a variety of monolayer materials, revealing the rich photonic properties that emerge with atomic-scale architecting and ‘defects by design’.

## Methods

**Sample Preparation:** 2.5  $\mu\text{L}$  of hBN nanoflakes (each flake 1-5 monolayers) in ethanol-water solution (Graphene Supermarket) is dropcast on cleaned holey carbon TEM grid (Quantifoil 0.6/1). The samples are dried in a vacuum bell jar at 80 °C for 30 minutes and annealed for 2 hours under ambient pressure and environment at low temperature (200-220°C) due to the stability of the ultra-thin carbon TEM substrate. Samples are stored in a glovebox under Ar.

**Optical Characterization:** The photoluminescence maps of the hBN nanoflakes are acquired using a Horiba confocal Raman microscope, with a 100x objective (NA = 0.6), an excitation laser power of  $\sim 100 \mu\text{W}$  at 532 nm, and a grating of 600 lines/mm groove density. The typical laser spot size is  $\sim 600\text{nm}$  and the acquisition time is 1 sec for each spectrum.

**Correlation  $g^{(2)}$  measurements:** Second-order autocorrelation measurements are performed using a Hanbury Brown and Twiss setup. The quantum emitter (QE) is excited by a 532 nm continuous wave laser through a laser line filter, and the photoluminescence from the QE is filtered by a dichroic filter (Semrock FF552-Di02-25x36) and a bandpass filter centered around the QE emission wavelength, and collected into a multi-mode fiber. The photoluminescence is directed towards a fiber beamsplitter; at the two output ports of the beamsplitter are two single-photon counting modules (SPCMs, Perkin-Elmer SPCM-AQR-14-FC). One SPCM is used as a start signal and the second used as a stop signal. By measuring the time delay between the two successive photon arrivals, a histogram of occurrences as a function of time delay is constructed. The photon counts were correlated using a PicoHarp300 time-correlated single-photon counting module, with a count rate of 10k cps and a typical integration time of 20 minutes for one dataset. For this measurement, the excitation laser power is kept below  $20\mu\text{W}$  to prevent degradation of both the emitters and the thin carbon film ( $\sim 12 \text{ nm}$ ) TEM grid.

**STEM-Cathodoluminescence characterization:** The electron microscope FEI Titan is operated at 80 kV. The Gatan Vulcan Cathodoluminescence TEM holder is used for light collection in STEM. The holder has two mirrors positioned above and below the sample. A hole of about  $500 \mu\text{m}$  in the mirrors allows the electron beam through. The reflected light is focused onto two optical fibers (multimode step index) and directed onto the photomultiplier tube (PMT) for panchromatic mapping or to the grating and CCD (cooled to  $-60^\circ\text{C}$ ) for spectral mapping. The two mirrors in the CL holder are focused and the collection window is  $200 \mu\text{m}$  in diameter. We use two fiber-coupled (multimode) LEDs (red and green) to align the two hotspots from the two mirrors after loading the sample.

The panchromatic photon pulse counting maps using the PMT are collected as  $512 \times 512$  pixels

and each pixel acquisition time is 60  $\mu$ s. For this mapping, C2 aperture is chosen to be 70  $\mu$ m (convergence semi angle is 14 mrad) and the STEM spot size (non monochromated) is chosen as either 6 or 7 (depending on the emitter intensity) and the screen current is 20 pA (spot size 7) or 40 pA (spot size 6). The spectral maps are collected using a 150 lines/mm grating and an acquisition times of 4s-8s per pixel, again depending on the intensity of the particular emitter. The spot size for this mapping is 6 and screen current is 40 pA. Software drift correction (after every 3 rows) is on during the collection. Samples are usually very stable with minimal drift. Dark corrections are performed at the end of collection of each maps. All mapping is done at room temperature.

**Correlation of optical and electron micrographs:** The TEM substrate is supported by a Au grid where each square in the grid is 40  $\mu$ m x 40  $\mu$ m. We focus on the central 4 squares, as those can be positioned to be in the CL holder optical hotspot ( $\sim 200\mu$ m in diameter). The 4 corners of each square serve as alignment markers for the region of interest; we note coordinates of each corner and each emitter region to triangulate distances from each corner. We take optical images of the entire square with a 100X objective and mark these regions with respect to the corners. Before STEM-CL imaging, we obtain TEM images at 70X-100X magnification (LM mode). We then use previously calculated distances from the corners and the 100X optical image to locate the regions of interest; this method is accurate to 1-2  $\mu$ m. For higher-accuracy mapping, we use a numbering system for the holes (i.e., recording the number of holes in  $x$  and  $y$  direction from any specific corner) to determine the appropriate position in the TEM. For localization beyond the diffraction limit, we collect STEM panchromatic-CL maps as described in Fig. 1(b). This method allows us to determine how many ‘bright’ emitters are located inside the  $\sim 500$  nm optical PL hotspot. Next we collect spectral signatures of each bright region as described in main text.

**NBED diffraction experiment:** The C2 aperture size is chosen as 10  $\mu$ m (convergence semi angle of 2 mrad), the spot size is 11, the screen current is  $\sim 1$  pA, each pixel acquisition time is 0.1 s, and each diffraction image is 4k x 4k.

**CL Spectral decomposition:** Spectral decomposition is performed using HyperSpy package in Python<sup>33</sup>. Any noise peaks are removed and the spectra are smoothed with LOWESS/ LOESS weighted regression algorithm using a smoothing parameter of 0.04. We perform principal component analysis (PCA) on the dataset to estimate the number of spectral components from the PCA weights. Finally, non-negative matrix factorization is performed with this number of spectral components to calculate the spectral weights and spectra.

**First Principles Calculations:** Multilayer hBN is modeled using DFT. Thermodynamic properties are calculated with appropriate charge correction (see SI for details). Shifts in transition energies with strain are determined to be optically allowed by analysis of the corresponding momentum matrix elements  $\langle \psi_i | \vec{p} | \psi_f \rangle$ . In order to capture the optically-relevant transitions in these defects, the HSE functional<sup>34</sup> was used with mixing parameter  $\alpha = 0.31$ , which has been shown to capture the  $\sim 6$  eV band gap of hBN with high accuracy<sup>30</sup>. Where appropriate, spin polarization is included. See SI for more details, including orbital diagrams and strain maps presented in SI Fig.

1.

1. Awschalom, D. D., Hanson, R., Wrachtrup, J. & Zhou, B. B. Quantum technologies with optically interfaced solid-state spins. *Nature Photonics* **12**, 516 (2018).
2. Atatüre, M., Englund, D., Vamivakas, N., Lee, S.-Y. & Wrachtrup, J. Material platforms for spin-based photonic quantum technologies. *Nature Reviews Materials* **3**, 38 (2018).
3. Wehner, S., Elkouss, D. & Hanson, R. Quantum internet: A vision for the road ahead. *Science* **362**, eaam9288 (2018).
4. Liao, S.-K. *et al.* Satellite-to-ground quantum key distribution. *Nature* **549**, 43 (2017).
5. Kucsko, G. *et al.* Nanometre-scale thermometry in a living cell. *Nature* **500**, 54 (2013).
6. Taylor, J. *et al.* High-sensitivity diamond magnetometer with nanoscale resolution. *Nature Physics* **4**, 810 (2008).
7. Aslam, N. *et al.* Nanoscale nuclear magnetic resonance with chemical resolution. *Science* **357**, 67–71 (2017).
8. Tran, T. T., Bray, K., Ford, M. J., Toth, M. & Aharonovich, I. Quantum emission from hexagonal boron nitride monolayers. *Nature Nanotechnology* **11**, 37 (2016).
9. Jungwirth, N. R. *et al.* Temperature dependence of wavelength selectable zero-phonon emission from single defects in hexagonal boron nitride. *Nano Letters* **16**, 6052–6057 (2016).
10. Grosso, G. *et al.* Tunable and high-purity room temperature single-photon emission from atomic defects in hexagonal boron nitride. *Nature Communications* **8**, 705 (2017).
11. Sontheimer, B. *et al.* Photodynamics of quantum emitters in hexagonal boron nitride revealed by low-temperature spectroscopy. *Physical Review B* **96**, 121202 (2017).
12. Exarhos, A. L., Hopper, D. A., Grote, R. R., Alkauskas, A. & Bassett, L. C. Optical signatures of quantum emitters in suspended hexagonal boron nitride. *ACS nano* **11**, 3328–3336 (2017).
13. Martínez, L. *et al.* Efficient single photon emission from a high-purity hexagonal boron nitride crystal. *Physical Review B* **94**, 121405 (2016).
14. Tran, T. T. *et al.* Robust multicolor single photon emission from point defects in hexagonal boron nitride. *ACS nano* **10**, 7331–7338 (2016).
15. Choi, S. *et al.* Engineering and localization of quantum emitters in large hexagonal boron nitride layers. *ACS applied materials & interfaces* **8**, 29642–29648 (2016).
16. Chejanovsky, N. *et al.* Structural attributes and photodynamics of visible spectrum quantum emitters in hexagonal boron nitride. *Nano letters* **16**, 7037–7045 (2016).

17. Jungwirth, N. R. & Fuchs, G. D. Optical absorption and emission mechanisms of single defects in hexagonal boron nitride. *Physical review letters* **119**, 057401 (2017).
18. Schell, A. W., Svedendahl, M. & Quidant, R. Quantum emitters in hexagonal boron nitride have spectrally tunable quantum efficiency. *Advanced Materials* **30**, 1704237 (2018).
19. Feng, J. *et al.* Imaging of optically active defects with nanometer resolution. *Nano letters* **18**, 1739–1744 (2018).
20. Bourrellier, R. *et al.* Bright uv single photon emission at point defects in h-bn. *Nano letters* **16**, 4317–4321 (2016).
21. Alem, N. *et al.* Atomically thin hexagonal boron nitride probed by ultrahigh-resolution transmission electron microscopy. *Physical Review B* **80**, 155425 (2009).
22. Jin, C., Lin, F., Suenaga, K. & Iijima, S. Fabrication of a freestanding boron nitride single layer and its defect assignments. *Physical Review Letters* **102**, 195505 (2009).
23. Wong, D. *et al.* Characterization and manipulation of individual defects in insulating hexagonal boron nitride using scanning tunnelling microscopy. *Nature nanotechnology* **10**, 949 (2015).
24. Lin, W.-H. *et al.* Atomic-scale structural and chemical characterization of hexagonal boron nitride layers synthesized at the wafer-scale with monolayer thickness control. *Chemistry of Materials* **29**, 4700–4707 (2017).
25. Barja, S. *et al.* Identifying substitutional oxygen as a prolific point defect in monolayer transition metal dichalcogenides with experiment and theory. *arXiv preprint arXiv:1810.03364* (2018).
26. Cassabois, G., Valvin, P. & Gil, B. Hexagonal boron nitride is an indirect bandgap semiconductor. *Nature Photonics* **10**, nphoton–2015 (2016).
27. Xue, Y. *et al.* Anomalous pressure characteristics of defects in hexagonal boron nitride flakes. *ACS nano* **12**, 7127–7133 (2018).
28. Reimers, J. R., Sajid, A., Kobayashi, R. & Ford, M. J. Understanding and calibrating density-functional-theory calculations describing the energy and spectroscopy of defect sites in hexagonal boron nitride. *Journal of chemical theory and computation* **14**, 1602–1613 (2018).
29. Tian, X. *et al.* Correlating 3d crystal defects and electronic properties of 2d materials at the single-atom level. *arXiv:1901.00633 [cond-mat]* (2019). URL <http://arxiv.org/abs/1901.00633>. ArXiv: 1901.00633.
30. Weston, L., Wickramaratne, D., Macko, M., Alkauskas, A. & Van de Walle, C. G. Native point defects and impurities in hexagonal boron nitride. *Physical Review B* **97** (2018). URL <https://link.aps.org/doi/10.1103/PhysRevB.97.214104>.

31. Abdi, M., Chou, J.-P., Gali, A. & Plenio, M. B. Color Centers in Hexagonal Boron Nitride Monolayers: A Group Theory and Ab Initio Analysis. *ACS Photonics* **5**, 1967–1976 (2018). URL <https://doi.org/10.1021/acsp Photonics.7b01442>.
32. Tawfik, S. A. *et al.* First-principles investigation of quantum emission from hBN defects. *Nanoscale* **9**, 13575–13582 (2017). URL <http://pubs.rsc.org/en/content/articlelanding/2017/nr/c7nr04270a>.
33. de la Pea, F. *et al.* hyperspy/ hyperspy v1.4.1 (2018). URL <https://doi.org/10.5281/zenodo.1469364>.
34. Heyd, J., Scuseria, G. E. & Ernzerhof, M. Erratum: “Hybrid functionals based on a screened Coulomb potential” [J. Chem. Phys. 118, 8207 (2003)]. *The Journal of Chemical Physics* **124**, 219906 (2006). URL <https://aip.scitation.org/doi/abs/10.1063/1.2204597>.

**Correspondence** Correspondence and requests for materials should be addressed to F. H. and J. A. D.